

# What is the origin of the intermediate-temperature magnetic specific heat capacity in the spin-liquid candidate $\text{Ca}_{10}\text{Cr}_7\text{O}_{28}$ ?

Joe Crossley\* and Chris Hooley†

SUPA, School of Physics & Astronomy, University of St Andrews,  
North Haugh, St Andrews, Fife KY16 9SS, U.K.

(Dated: September 26, 2023)

We present several approximate calculations of the specific heat capacity of the model for  $\text{Ca}_{10}\text{Cr}_7\text{O}_{28}$  proposed by Balz *et al.* [Phys. Rev. B **95**, 174414 (2017)], using methods including exact diagonalization, Thermal Pure Quantum States, and high-temperature expansions. In none of these cases are we able to reproduce the magnitude of the zero-field specific heat capacity shown in the intermediate-temperature ( $\sim 5 - 15\text{K}$ ) experimental data. We discuss possible reasons for the discrepancy, and what it might tell us about the magnetic Hamiltonian for  $\text{Ca}_{10}\text{Cr}_7\text{O}_{28}$ .

## I. INTRODUCTION

This year marks the 50<sup>th</sup> anniversary of Anderson’s famous suggestion [1] that the ground state of the spin-1/2 Heisenberg model on the triangular lattice might be a resonating valence bond state. Despite the now convincing evidence that the ground state of that particular model has Néel order [2–4], Anderson’s proposal — together with the discovery thirteen years later of the high- $T_c$  cuprate family of materials [5, 6] — provoked an interest in the study of so-called ‘spin liquid’ phases which persists to this day [7, 8].

One candidate spin liquid material that has given rise to considerable interest over the past few years is  $\text{Ca}_{10}\text{Cr}_7\text{O}_{28}$ . Balz *et al.* have suggested a two-dimensional model [9–12], while Alshalawi *et al.* recently proposed a 3D description [13]. Both of these sets of authors attribute the magnetic behavior of  $\text{Ca}_{10}\text{Cr}_7\text{O}_{28}$  to the six  $\text{Cr}^{5+}$  ions in each formula unit [10]. These are arranged in distorted kagome planes, with each site hosting a well-localized spin-1/2 degree of freedom.

The model proposed by Balz *et al.* is known as the breathing bilayer kagome (BBK) Hamiltonian,

$$\hat{H} = \sum_{\langle i,j \rangle} J_{ij} \hat{\mathbf{S}}_i \cdot \hat{\mathbf{S}}_j - g\mu_B h \sum_i \hat{S}_i^z, \quad (1)$$

where  $\langle i,j \rangle$  denotes summation over nearest neighbor bonds (counting each bond only once),  $h$  denotes the applied magnetic field strength, and the  $g$ -factor is taken to be 2. This 2D model couples kagome layers into bilayers as shown in Fig. 1. The term ‘breathing’ refers to the inequivalence of triangles within each kagome plane. The couplings themselves are of weak Heisenberg type, and have mixed ferro-/antiferromagnetic nature. Their numerical values, given by Balz *et al.*, are included in Fig. 1; Balz *et al.* determined these by fitting the structure factor of the model to the spin-wave spectrum of  $\text{Ca}_{10}\text{Cr}_7\text{O}_{28}$  under a high magnetic field. Theoretical

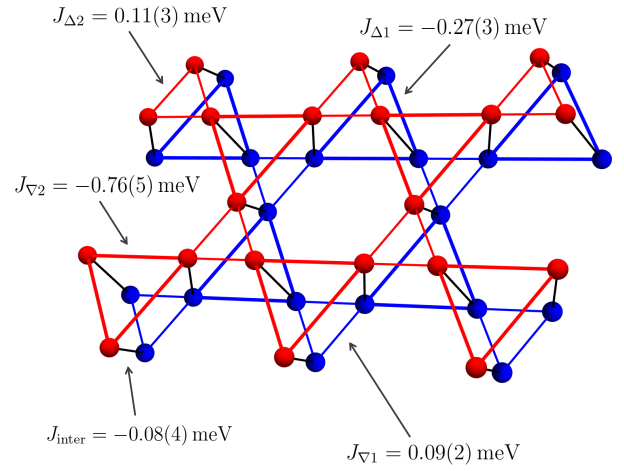


FIG. 1. A section from a single bilayer of  $\text{Ca}_{10}\text{Cr}_7\text{O}_{28}$ . The blue and red spheres denote  $\text{Cr}^{5+}$  ions from layers 1 and 2 respectively. All distinct couplings in the breathing bilayer kagome model are indicated by their symbol and associated value, as determined by Balz *et al.* in ref. [11].

studies suggest that this model does indeed exhibit spin liquid behavior at the lowest temperatures [12, 14–16].

In this paper, we present evidence that the BBK model is appreciably incomplete as a description of the magnetism of  $\text{Ca}_{10}\text{Cr}_7\text{O}_{28}$ . We are not the first to raise concerns along these lines; Pohle *et al.* [14] noted that the presence of finite-energy scattering weight at  $\mathbf{q} = \mathbf{0}$  in zero-field neutron scattering experiments implies that there is significant anisotropy in the exchange interactions, a feature that the model (1) does not reproduce. We have sought to further test this model by using various methods to calculate its specific heat capacity (with and without a 12 T field), magnetization, and magnetic susceptibility, and cross-checking with experiment. Inconsistency between the model and experiment is most clearly seen in the zero-field specific heat capacity data, so this is where we will focus our discussion. Balz *et al.* also discuss, though ultimately discard, an alternative model called the ‘coupled hexagon model’ [10].

\* jc413@st-andrews.ac.uk (corresponding author)

† cah19@st-andrews.ac.uk

This model, too, appears unable to reproduce the specific heat capacity of  $\text{Ca}_{10}\text{Cr}_7\text{O}_{28}$  (results presented in Supplemental Material).

The remainder of this paper is structured as follows. In Section II, we present the results of four different methods used to approximately calculate the specific heat capacity of the BBK model: the strong-triangle model (an approximation based on the hierarchy of coupling strengths), exact diagonalization, Thermal Pure Quantum States, and the high-temperature expansion. In Section III we discuss our results, and the modifications to the magnetic model of  $\text{Ca}_{10}\text{Cr}_7\text{O}_{28}$  that they might suggest.

## II. RESULTS

### A. Strong-Triangle Model

We expect something of a separation of scales in the BBK model since the  $J_{\Delta 1}$  and  $J_{\nabla 2}$  couplings stand out as stronger than the rest. This allows one to calculate the dominant contribution to the high-temperature specific heat capacity by switching off all other couplings, leaving isolated ‘strong triangles’. Having couplings of  $J_{\Delta 1}$  and  $J_{\nabla 2}$ , these ferromagnetic trios of spins have a gap between their ground state (spin-3/2) manifold and their excited (spin-1/2) manifold of  $3|J_{\Delta 1}|/2$  and  $3|J_{\nabla 2}|/2$  respectively. Thus, an approximation to the specific heat capacity in the thermodynamic limit can be calculated quickly and easily.

We show our results in Fig. 2 for the 0 T and 12 T specific heat capacities calculated using this technique. Clearly the approximation works fairly well in the presence of a 12 T field. We expect this to be the case as the gap between eigenstates is well accounted for by the Zeeman and stronger ferromagnetic terms alone. In the absence of any external field, on the other hand, gaps between the lowest energy eigenstates occur only if we include the weaker bonds. Thus, our strong-triangle model cannot correctly reproduce the zero-field specific heat capacity at the lowest temperatures. This is no surprise; more concerningly, however, it shows significant disagreement with the experimental data even in the intermediate temperature range (5–15 K). Could this be due purely to the omission of the weaker exchange couplings, or must other physics be invoked to account for it?

### B. Exact Diagonalization

In an initial attempt to recover something of the weak coupling physics we now ‘switch on’  $J_{\nabla 1}$  and  $J_{\Delta 2}$ , neglecting only  $J_{\text{inter}}$ . This enables a simple exact diagonalization description where one diagonalizes a cluster of spins in each layer and then combines their spectra to calculate the specific heat capacity (see Supplemental Material for cluster dimensions).

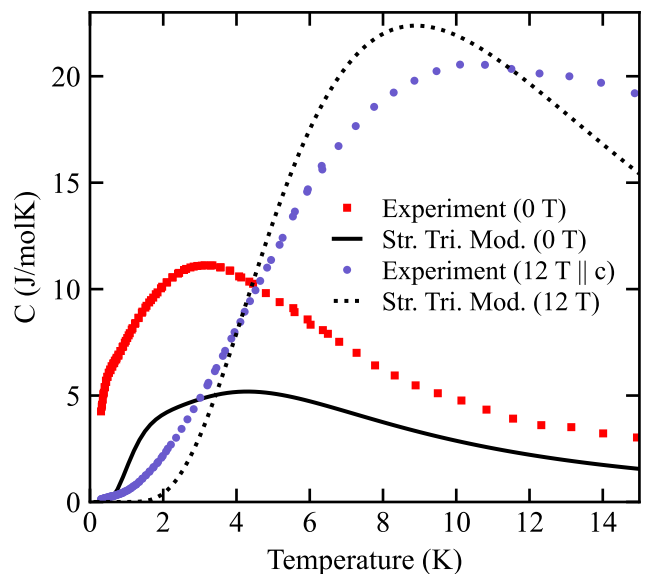


FIG. 2. The specific heat capacity of the breathing bilayer kagome model (1) using the strong-triangle approximation, in zero magnetic field (solid black curve) and in a magnetic field of 12 T (dotted black curve). Experimental data, previously published in ref. [11], are also shown for comparison.

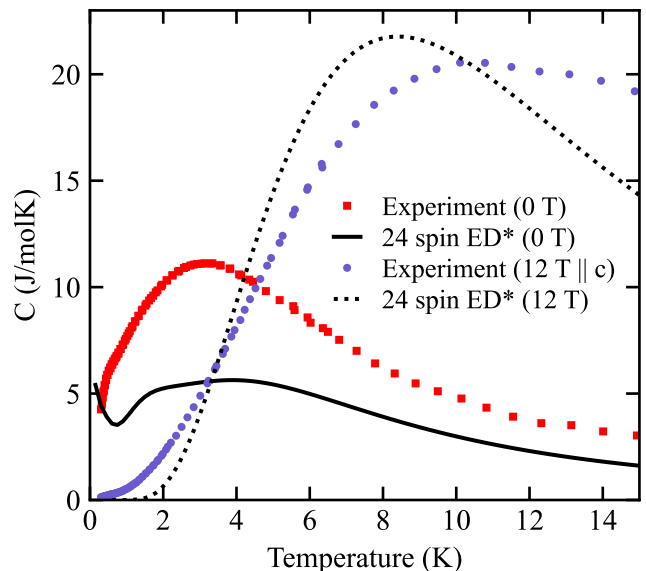


FIG. 3. The specific heat capacity of the breathing bilayer kagome model (1) calculated using exact diagonalization of a cluster of 24 spins (12 per layer), in zero magnetic field (solid black curve) and in a magnetic field of 12 T (dotted black curve). ‘ED\*’ denotes that the exact diagonalization was performed with  $J_{\text{inter}} = 0$ . Experimental data, previously published in ref. [11], are shown for comparison.

We show our results for a cluster of 24 spins in Fig. 3. Comparison with Fig. 2 confirms that the inclusion of  $J_{\nabla 1}$  and  $J_{\Delta 2}$  causes no significant change to the 12 T curve. The story is somewhat similar for the zero-field

curve, which appears to exactly follow that of the strong-triangle model down to  $\sim 4$  K, and still falls far short of the experimental specific heat capacity across almost the entire measured temperature range. We now turn to two more powerful techniques where all couplings are properly accounted for.

### C. Thermal Pure Quantum States

The method of canonical Thermal Pure Quantum States (TPQS) was introduced by Sugiura and Shimizu [17]. Fundamentally approximate, it can be used as an alternative to exact diagonalization, enabling larger cluster sizes to be treated. The method works by selecting a random vector in the many-body Hilbert space and using this pure state as a kind of proxy for the true infinite-temperature mixed state. This ‘thermal state’ is cooled down step-by-step by acting an adapted version of the Hamiltonian upon it (namely  $l - \hat{H}/N$ , where  $N$  is the number of lattice sites, and  $l$  is an upper bound on the eigenvalue spectrum of  $\hat{H}/N$ ). By taking expectation values at each iteration, thermodynamic variables (such as the specific heat capacity) can be calculated as functions of temperature.

Sugiura and Shimizu present a scheme for calculating the uncertainty associated with the method—the degree to which the result could be expected to differ from that of an exact diagonalization calculation. In all cases the uncertainty margin at each temperature never exceeds  $\sim 1\%$ . We also bench-marked our code against the data of Elstner and Young for the spin-1/2 Heisenberg antiferromagnet on the kagome lattice [18] (see Supplemental Material).

Fig. 4 shows the zero-field TPQS specific heat capacity of (1) for clusters of 18, 24, and 30 spins (see Supplemental Material for exact cluster dimensions). The TPQS method becomes more accurate for larger Hilbert spaces. In the 30-spin case a single TPQS run was sufficient but for smaller clusters we averaged our results over several runs to bring our uncertainty measures down: eight runs for the 24-spin case and 100 runs for the 18-spin case. Our results were obtained by parallelizing the calculation across 64 cores of one of the nodes in the Edinburgh SGE cluster. Due to memory considerations, we successively generated the matrix elements of the Hamiltonian rather than storing them all simultaneously.

For spin clusters of these sizes, the separation of coupling strengths in the model (1) is clearly manifest in the two distinct peaks in the specific heat capacity. No such double-peak structure is seen in the experimental data.

### D. High-Temperature Expansion

The high-temperature expansion (HTE) can be used to calculate the specific heat capacity in the thermodynamic limit as a power series in  $J/(k_B T)$  [20]. The expan-

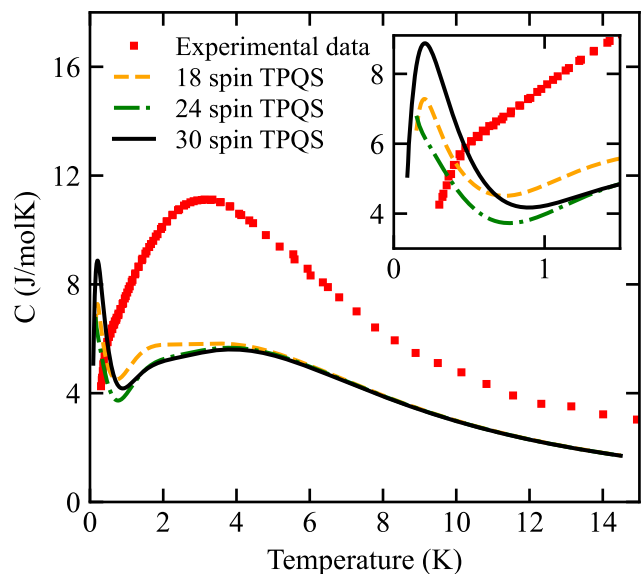


FIG. 4. The specific heat capacity of the breathing bilayer kagome model (1) calculated using Thermal Pure Quantum States for clusters of 18, 24, and 30 spins, in the absence of a magnetic field. For 18 spins we averaged across 100 runs, for 24 spins we averaged across eight runs, and for 30 spins only a single run was used. In all cases the uncertainty margin at each temperature never exceeds  $\sim 1\%$ . The experimental zero-field specific heat capacity of  $\text{Ca}_{10}\text{Cr}_7\text{O}_{28}$ , previously published in ref. [11], is also shown. For clarity, we have included an inset which enlarges the heat capacity curves at the lowest temperatures.

sion coefficients can be calculated as traces over products of operators appearing in the Hamiltonian. These ‘moments’ become increasingly complex for higher orders.

Following ref. [21], we calculated the first five moments for the heat capacity of (1) by hand. The C++ package by Lohmann *et al.* [19] enabled us to further calculate the series up to tenth order, as well as providing three different Padé approximants to extend the series. The package only allows for four different coupling strengths, so we set  $J_{\nabla_1} = J_{\Delta_2}$  (which is in any case consistent with the quoted uncertainties in these coupling constants) to go from five different coupling strengths to four.

We show our results in Fig. 5 along with the experimental zero-field specific heat capacity and the 30-spin TPQS curve for comparison. Our finite-order results diverge at low temperatures as is normal for such series. Assuming further orders in the expansion are well behaved, one typically decides the temperature down to which such curves can be trusted by looking for the point at which consecutive orders separate appreciably from one another. The geometry of the BBK lattice gives no specific reason to expect the higher-order terms to be poorly behaved, so we take the ninth- or tenth-order curves as essentially correct down to  $\sim 9$  K.

The three Padé approximants agree down to even lower temperatures. These approximants are quotients of

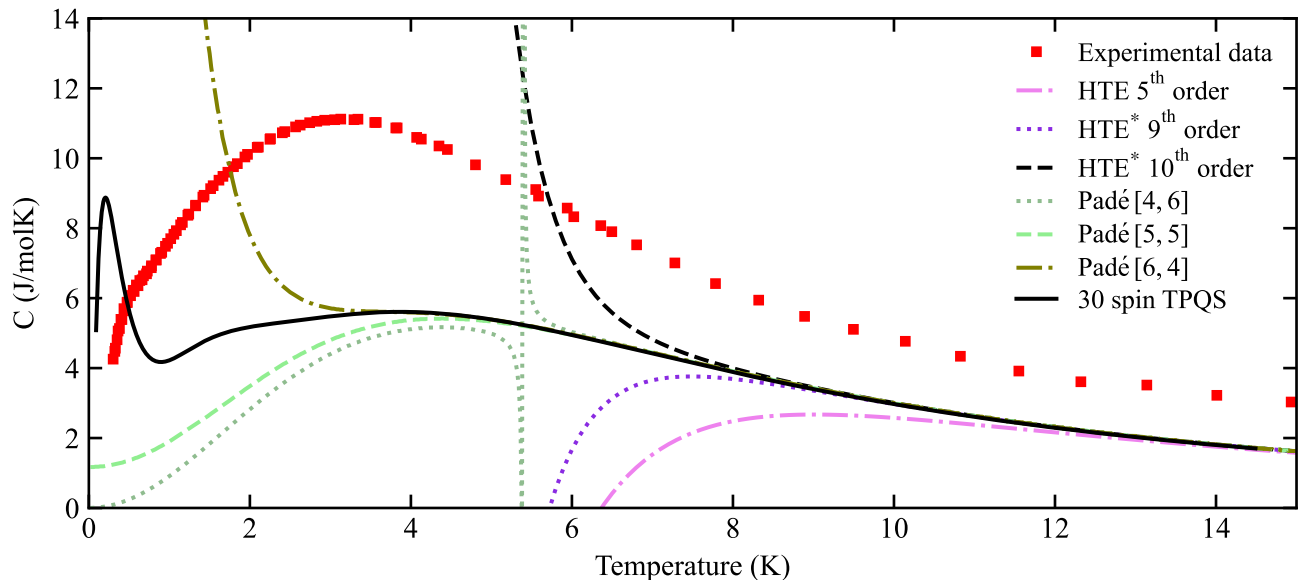


FIG. 5. The specific heat capacity of the breathing bilayer kagome model (1) in the absence of a magnetic field, calculated using the high-temperature expansion to various orders as stated in the legend. The curves labelled “HTE\*” were calculated using a software package [19] allowing only four different coupling strengths, meaning we set  $J_{\nabla 1} = J_{\Delta 2}$  (which is in any case consistent with the quoted uncertainties in these coupling constants). The various Padé curves were also computed using the aforementioned software package; they are based on the 10<sup>th</sup> order expansion obtained by the software, labelled here as “HTE\* 10<sup>th</sup> order”. For comparison, we show our 30-spin Thermal Pure Quantum States curve for the model, as well as the experimental zero-field specific heat capacity data previously published in ref. [11].

polynomials in  $J/(k_B T)$  and we label them Padé  $[L, M]$ , where  $L$  is the polynomial order of the numerator and  $M$  is the polynomial order of the denominator. A ‘complete’ approximation to the heat capacity should converge to zero as  $T \rightarrow 0$ ; this is only guaranteed for approximants where  $L < M$  [18]. Yet, our curve for which this condition is satisfied (Padé  $[4, 6]$ ) exhibits a dramatic singularity at intermediate temperatures. Comparison with the other approximants, as well as with the TPQS curve, suggests that this is a “spurious pole” (a well-known effect where the Padé approximant exhibits a pole that is not a feature of the target function). In any case, we find the three approximants in good agreement with one another right down to  $\sim 6$  K.

### III. DISCUSSION

The strong-triangle model is clearly a drastic approximation, especially in the absence of a magnetic field. Even so, it is very useful: the one who believes that  $\text{Ca}_{10}\text{Cr}_7\text{O}_{28}$  is described by the BBK model (1) is forced to say that the weak couplings would, were they included, account for the difference between the calculated and measured specific heat capacities of Fig. 2. This requires that the weak couplings strongly enhance the specific heat capacity far beyond their temperature scale of  $\sim 1$  K, which intuitively seems unlikely given the structure of the model. To test this intuition we undertook three further calculations, all of which sought to include

the effect of the weaker couplings.

Our exact diagonalization method includes all but one of the weaker coupling types, and the TPQS method includes them all. As expected, these weaker couplings lead to no noticeable change in the specific heat capacity right down to  $\sim 4$  K; rather, a second peak emerges below 1 K, increasing the apparent disparity between theory and experiment. Yet both methods are subject to finite-size effects. We might question whether longer-range physics would push this new low-temperature peak upward to supplement the broader peak at  $\sim 4$  K — from an entropic perspective, this peak-migration effect could account for the difference between theory and experiment (see Supplemental Material).

To address the issue of potential finite-size effects we now turn to our final technique, the high-temperature expansion, which allows us to calculate the specific heat capacity in the thermodynamic limit. The ninth- and tenth-order HTEs follow our 30-spin TPQS curve down to  $\sim 9$  K (below which we argue they are no longer valid anyway), and all the Padé extensions follow our 30-spin TPQS curve down to  $\sim 6$  K. Thus, despite finite-size effects, we claim that the 30-spin TPQS curve suitably reproduces the specific heat capacity of the BBK model (1) in the thermodynamic limit, right down to  $\sim 6$  K.

We are left with an apparent disparity between theory and experiment; what are we to make of it? One might seek a resolution by claiming that there remains a residual phononic contribution in the experimental data. The size of the discrepancy, and the fact it appears to be

strongly dependent on the applied magnetic field, make it unlikely that this is the full story. Therefore, taken together with Pohle *et al.*'s argument for anisotropy (see introduction), these calculations provide a strong incentive to explore improvements to the BBK model for  $\text{Ca}_{10}\text{Cr}_7\text{O}_{28}$ .

A weak Dzyaloshinskii-Moriya interaction [22] would break the degeneracy of the ground state manifold of each of the strong triangles, leaving only a Kramers doublet in its place. This could be the mechanism by which the entropy under the low temperature peak is moved to supplement the broader peak at higher temperatures. While such anisotropic interactions are not usually essential to describe the magnetism of 3d transition metal ions, the quoted strengths of the Heisenberg interactions in the BBK model are themselves so weak that lower symmetry effects need not be that great before they become important. One might oppose the suggestion of anisotropy by pointing to the similarity of the magnetic susceptibility curves of Balz *et al.* [11] when the field is applied along different crystal axis directions. However, local anisotropic effects in competition can conspire to produce exactly such behavior [23].

We are currently using a variational approach based on the addition of general anisotropic exchange terms to

the strong-triangle model, fitting to the wealth of experimental data available. While our plan is initially to focus on the strong bonds in the model, we hope this will also function to improve the accuracy of the model down to the lowest temperatures [23].

## ACKNOWLEDGMENTS

The authors would like to thank Christian Balz, Bella Lake, and Nic Shannon for helpful discussions, and Christian Balz and Bella Lake for kindly sharing the original specific heat capacity data published in ref. [11]. We also thank A. Lohmann, J. Richter, and H.-J. Schmidt for their excellent C++ package for computing high-temperature expansions [19], which can be found at <http://www.uni-magdeburg.de/jschulen/HTE10/>. All Thermal Pure Quantum States calculations were performed on the Edinburgh University SGE cluster.

JAC acknowledges support from UKRI via EPSRC grant EP/T518062/1. CAH acknowledges support from UKRI via EPSRC grant EP/R031924/1.

This work was performed in part at Aspen Center for Physics, which is supported by National Science Foundation grant PHY-2210452.

- 
- [1] P. W. Anderson, Resonating valence bonds: A new kind of insulator?, *Mater. Res. Bull.* **8**, 153 (1973).
  - [2] T. Jolicoeur and J. C. Le Guillou, Spin-wave results for the triangular Heisenberg antiferromagnet, *Phys. Rev. B* **40**, 2727 (1989).
  - [3] B. Bernu, P. Lecheminant, C. Lhuillier, and L. Pierre, Exact spectra, spin susceptibilities, and order parameter of the quantum Heisenberg antiferromagnet on the triangular lattice, *Phys. Rev. B* **50**, 10048 (1994).
  - [4] L. Capriotti, A. E. Trumper, and S. Sorella, Long-range Néel Order in the Triangular Heisenberg Model, *Phys. Rev. Lett.* **82**, 3899 (1999).
  - [5] J. G. Bednorz and K. A. Müller, Possible high  $T_c$  superconductivity in the Ba-La-Cu-O system, *Z. Phys. B* **64**, 189 (1986).
  - [6] M.-K. Wu, J. R. Ashburn, C. Torng, P.-H. Hor, R. L. Meng, L. Gao, Z. J. Huang, Y. Wang, and a. Chu, Superconductivity at 93 K in a new mixed-phase Y-Ba-Cu-O compound system at ambient pressure, *Phys. Rev. Lett.* **58**, 908 (1987).
  - [7] L. Savary and L. Balents, Quantum spin liquids: a review, *Rep. Prog. Phys.* **80**, 016502 (2016).
  - [8] C. Broholm, R. Cava, S. Kivelson, D. Nocera, M. Norman, and T. Senthil, Quantum spin liquids, *Science* **367**, eaay0668 (2020).
  - [9] C. Balz, B. Lake, J. Reuther, H. Luetkens, R. Schönemann, T. Herrmannsdörfer, Y. Singh, A. T. M. Nazmul Islam, E. M. Wheeler, J. A. Rodriguez-Rivera, T. Guidi, G. G. Simeoni, C. Baines, and H. Ryll, Physical realization of a quantum spin liquid based on a complex frustration mechanism, *Nature Physics* **12**, 942 (2016).
  - [10] C. Balz, B. Lake, M. Reehuis, A. T. M. Nazmul Islam, O. Prokhnenko, Y. Singh, P. Pattison, and S. Tóth, Crystal growth, structure and magnetic properties of  $\text{Ca}_{10}\text{Cr}_7\text{O}_{28}$ , *J. Phys. Condens. Matter* **29**, 225802 (2017).
  - [11] C. Balz, B. Lake, A. T. M. Nazmul Islam, Y. Singh, J. A. Rodriguez-Rivera, T. Guidi, E. M. Wheeler, G. G. Simeoni, and H. Ryll, Magnetic Hamiltonian and phase diagram of the quantum spin liquid  $\text{Ca}_{10}\text{Cr}_7\text{O}_{28}$ , *Phys. Rev. B* **95**, 174414 (2017).
  - [12] J. Sonnenschein, C. Balz, U. Tutsch, M. Lang, H. Ryll, J. A. Rodriguez-Rivera, A. T. M. Nazmul Islam, B. Lake, and J. Reuther, Signatures for spinons in the quantum spin liquid candidate  $\text{Ca}_{10}\text{Cr}_7\text{O}_{28}$ , *Phys. Rev. B* **100**, 174428 (2019).
  - [13] D. R. Alshalawi, J. M. Alonso, A. R. Landa-Cánovas, and P. de la Presa, Coexistence of Two Spin Frustration Pathways in the Quantum Spin Liquid  $\text{Ca}_{10}\text{Cr}_7\text{O}_{28}$ , *Inorg. Chem.* **61**, 16228 (2022).
  - [14] R. Pohle, H. Yan, and N. Shannon, Theory of  $\text{Ca}_{10}\text{Cr}_7\text{O}_{28}$  as a bilayer breathing-kagome magnet: Classical thermodynamics and semiclassical dynamics, *Phys. Rev. B* **104**, 024426 (2021).
  - [15] A. Kshetrimayum, C. Balz, B. Lake, and J. Eisert, Tensor network investigation of the double layer Kagome compound  $\text{Ca}_{10}\text{Cr}_7\text{O}_{28}$ , *Ann. Phys.* **421**, 168292 (2020).
  - [16] S. Biswas and K. Damle, Semiclassical theory for liquid-like behavior of the frustrated magnet  $\text{Ca}_{10}\text{Cr}_7\text{O}_{28}$ , *Phys. Rev. B* **97**, 115102 (2018).
  - [17] S. Sugiura and A. Shimizu, Canonical Thermal Pure Quantum State, *Phys. Rev. Lett.* **111**, 010401 (2013).
  - [18] N. Elstner and A. Young, Spin-1/2 Heisenberg antiferro-

- magnet on the *kagomé* lattice: High-temperature expansion and exact-diagonalization studies, Phys. Rev. B **50**, 6871 (1994).
- [19] A. Lohmann, H.-J. Schmidt, and J. Richter, Tenth-order high-temperature expansion for the susceptibility and the specific heat of spin- $s$  Heisenberg models with arbitrary exchange patterns: Application to pyrochlore and kagome magnets, Phys. Rev. B **89**, 014415 (2014).
- [20] J. Oitmaa, C. Hamer, and W. Zheng, *Series Expansion Methods for Strongly Interacting Lattice Models* (Cambridge University Press, 2006).
- [21] H.-J. Schmidt, A. Lohmann, and J. Richter, Eighth-order high-temperature expansion for general Heisenberg Hamiltonians, Phys. Rev. B **84**, 104443 (2011).
- [22] S. Blundell, *Magnetism in Condensed Matter* (OUP Oxford, 2001).
- [23] J. A. Crossley and C. A. Hooley, in preparation.
- [24] <https://automeris.io/WebPlotDigitizer/>.
- [25] <https://www.wolfram.com/mathematica/>.

## Supplemental Material for “What is the origin of the intermediate-temperature magnetic specific heat capacity in the spin-liquid candidate $\text{Ca}_{10}\text{Cr}_7\text{O}_{28}$ ?”

### I. DEFINING A UNIT CELL

In order to make direct comparison with the published experimental specific heat capacity of Balz *et al.* we had to adopt the same definition of the unit cell.

To do this, we referred to the magnetic specific heat capacity reported in Fig. 2(c) of ref. [11]. Integrating  $C/T$  between  $T = 0$  and  $T \rightarrow \infty$ , one would obtain the change in molar magnetic entropy in bringing the system out of its ground state manifold towards the high-temperature limit where every microstate is equally accessible. We focused on the 12 T case where there is a unique, fully-polarized ground state. For 12 T therefore, the *change* in molar entropy (in raising the temperature from 0 K to the infinite limit) is equal to the *total* molar entropy of the system.

Using WebPlotDigitizer [24], we extracted the high-field data from Fig. 2(c) of ref. [11]. Using Mathematica [25], we converted the data to  $C/T$ , created a continuous curve using the ‘Interpolate’ function, and then performed numerical integration and simultaneous extrapolation up to 23 K (in order to approximately capture as much of the available entropy of the system as possible) using ‘NIntegrate’. From this we deduced a total entropy change of  $\sim 33.5 \text{ J mol}^{-1} \text{ K}^{-1}$ . We expect the exact answer to be equal to  $nR \ln(2)$ , where  $R \ln(2)$  is the maximum available entropy per mole of a given spin- $\frac{1}{2}$  site and  $n$  is the number of sites per unit cell. Dividing 33.5 by  $R \ln(2)$  we get  $\sim 5.8$  from which we may assume that  $n = 6$  (6 sites per unit cell). This coincides with the size of the unit cell for a single kagome bilayer of  $\text{Cr}^{5+}$  ions as shown in Fig. 1 of the main article.

## II. CALCULATION DETAILS

### A. Coupling parameters

Table I displays the different coupling values we used across this work. For the strong-triangle method we used column (a), for exact diagonalization we used column (b), for Thermal Pure Quantum States and the high-temperature expansion up to 5<sup>th</sup> order we used column (c), and for all other high-temperature expansion calculations we used column (d). Cases where we have set couplings to zero are clearly signposted in the main text. Otherwise, all coupling values used fall within the uncertainty margins for the couplings of the BBK model for  $\text{Ca}_{10}\text{Cr}_7\text{O}_{28}$  given by Balz *et al.* [11].

Coupling / meV	(a)	(b)	(c)	(d)
$J_{\Delta 1}$	-0.2730	-0.2730	-0.2730	-0.2730
$J_{\nabla 1}$	0	0.0920	0.0920	0.1025
$J_{\Delta 2}$	0	0.1130	0.1130	0.1025
$J_{\nabla 2}$	-0.7650	-0.7650	-0.7650	-0.7650
$J_{\text{inter}}$	0	0	-0.0840	-0.0840

TABLE I. The four different sets of coupling values used in the calculations throughout this work. Couplings are stated in units of meV.

### B. Cluster definitions

We have reported a range of calculations performed on finite clusters of spins with periodic boundary conditions. Fig. 6 (a) shows the clusters used in all calculations involving either 18 or 24 spins. Fig. 6 (b) shows the cluster used in all 30-spin calculations.

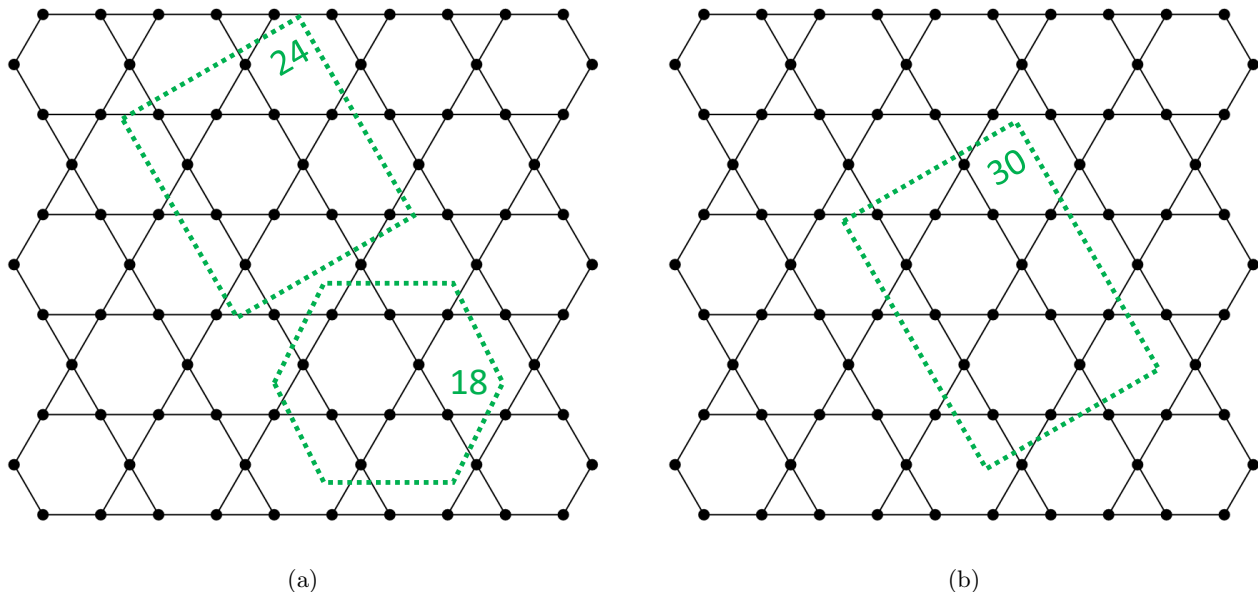


FIG. 6. Diagrams of the 18, 24, and 30-spin clusters used in all exact diagonalization and Thermal Pure Quantum States calculations throughout this paper. For clarity, only a single layer of the bilayer structure is shown; one should imagine each dotted boundary enclosing the same set of spins in the other layer also. The 24-spin cluster can tile space in two different ways but the resulting Hamiltonian is the same in both cases.

The 24-spin cluster can be used to tile the lattice in two different ways: checkered tiling (Fig. 7 (a)) and brick-wall tiling (Fig. 7 (b)).

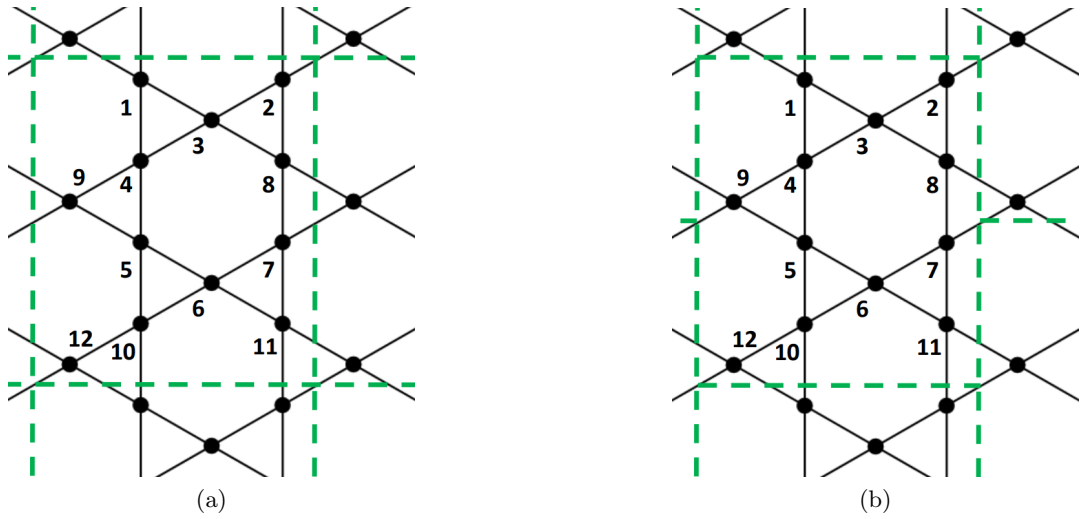


FIG. 7. The two alternative tilings of the 24-spin cluster outlined in Fig. 6 (a). We show a single layer of the bilayer structure for clarity, and we ascribe labels to the depicted spins in correspondence with the labels used in Fig. 8.

These two tilings simply differ by site labelling. To demonstrate this, Fig. 8 shows their corresponding connectivity.

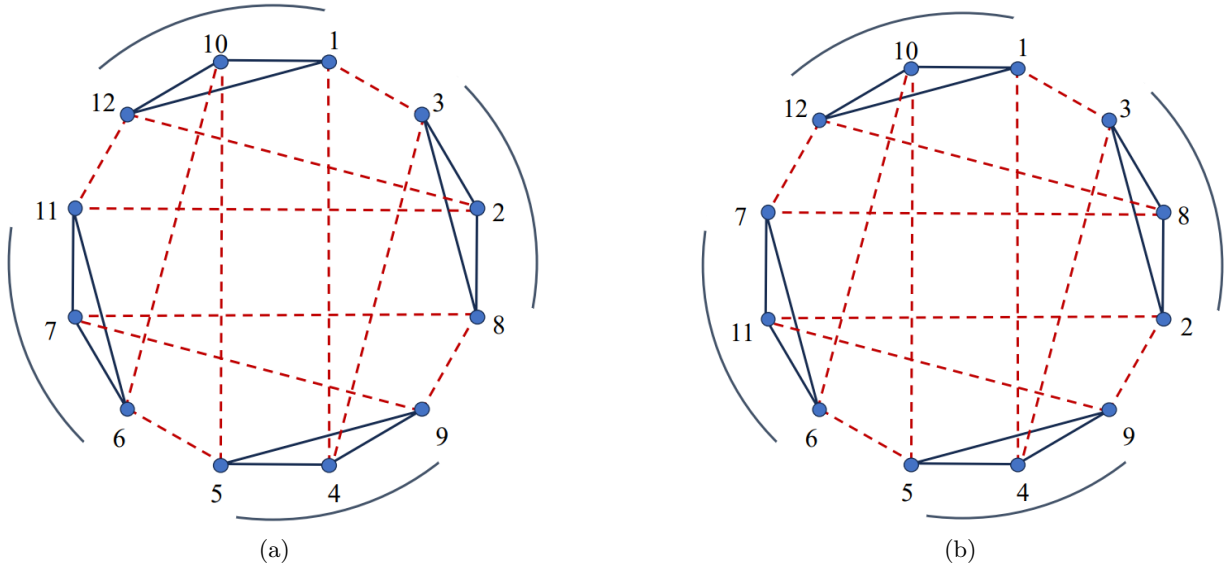


FIG. 8. Graphs showing the connectivity of a single layer of spins for the two alternative tilings of the 24-spin cluster outlined in Fig. 6 (a). Graph (a) corresponds to the checkerboard tiling of Fig. 7 (a), and graph (b) corresponds to the brick-wall tiling of Fig. 7 (b). Red hatched lines connecting vertices correspond to bonds within the right-pointing triangles of Fig. 7, while black lines connecting vertices correspond to bonds within the left-pointing triangles. The arcs surrounding each graph have been added to help elucidate the  $C_4$  symmetry.

### III. BENCHMARKING THE TPQS CODE

To benchmark our TPQS code we calculated the specific heat capacity for a cluster of 18 spin- $\frac{1}{2}$  moments on a kagome lattice interacting under nearest-neighbor antiferromagnetic Heisenberg interactions. This calculation has already been done exactly by Elstner and Young [18], enabling a direct comparison to be made. The uncertainties associated with using this technique for such a small cluster of spins are relatively high and so we chose to loop the algorithm 100 times, taking the average result. This lowered the uncertainty bounds on our results by a factor of ten. Fig. 9 demonstrates our results converging towards the exact diagonalization data as we average over successively more TPQS trials.

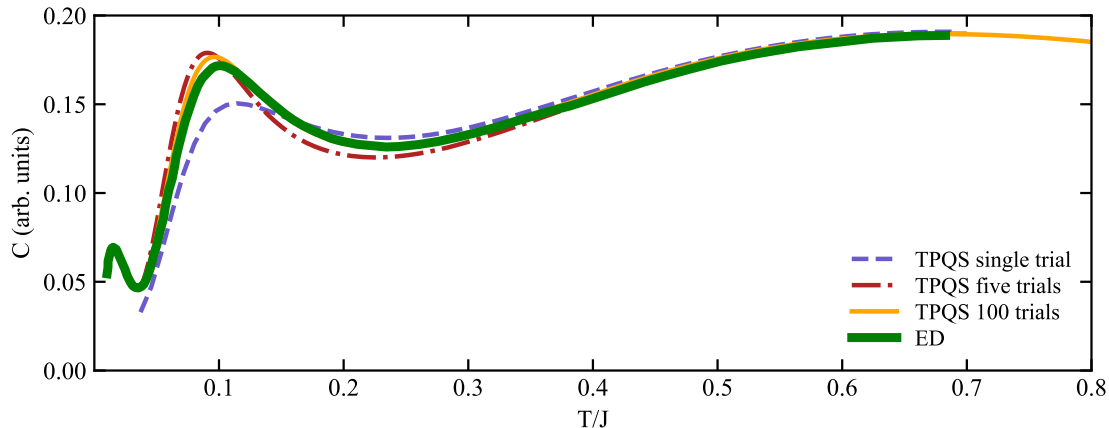


FIG. 9. The zero-field magnetic specific heat capacity of a cluster of 18 spin- $\frac{1}{2}$  moments under nearest-neighbor antiferromagnetic Heisenberg interactions on the kagome lattice. We show TPQS results for a single trial (blue dashed curve), a five-trial average (red dot-dashed curve), and a 100-trial average (yellow curve). The exact diagonalization data (green) of Elstner and Young [18] was copied using WebPlotDigitizer [24] and is shown here for comparison.

#### IV. AN ENTROPIC COMPARISON OF THEORY AND EXPERIMENT

In Fig. 10 we compare the  $C/T$  curve for our 30-spin TPQS calculation with that of experiment. The experimental curve was obtained by linear interpolation of data points copied from ref. [15] using WebPlotDigitizer [24]. The shaded areas labelled  $A$  and  $B$  correspond to differences in the entropy under each curve. Area  $A$  approximately corresponds to the surplus molar entropy in the 30-spin TPQS simulation (relative to the experiment) upon raising the temperature from 0.15 K to 0.45 K. Area  $B$  corresponds to the extra molar entropy unlocked in experiment (relative to the 30-spin TPQS simulation) upon raising the temperature from 0.45 K to 7 K. The two curves essentially converge beyond this point. These two areas appear roughly equal, and therefore the curves contain similar entropies as one would hope. However, this argument is hardly rigorous; we do not have sufficient data to see exactly how the two curves would bound the lower-temperature part of the area  $A$ .

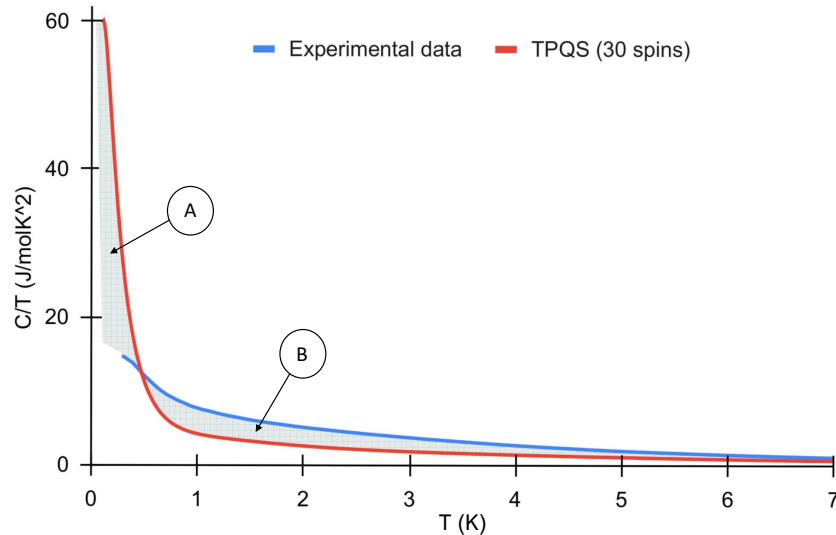


FIG. 10. A plot of the zero-field magnetic specific heat capacity divided by temperature for  $\text{Ca}_{10}\text{Cr}_7\text{O}_{28}$ . The experimental curve (blue) was obtained by linear interpolation of data points copied from ref. [15] using WebPlotDigitizer [24]. The two curves cross over at around  $T = 0.45$  K. We note that the entropy surplus in the TPQS simulation relative to the experiment at low temperatures ( $A$ ) appears to balance the entropy deficit at higher temperatures ( $B$ ).

## V. THE SPECIFIC HEAT CAPACITY OF THE COUPLED HEXAGON MODEL

Throughout this report we have considered the breathing bilayer kagome (BBK) model for  $\text{Ca}_{10}\text{Cr}_7\text{O}_{28}$  as presented by Balz *et al.* in ref. [9]. The same authors mention an alternative magnetic Hamiltonian for this material, called the coupled hexagon model [11]. These two models fit the high-field neutron scattering data for the real material equally well, yet the BBK model is favored on the basis of structural considerations. We chose to revisit the coupled hexagon model by calculating the specific heat capacity of a cluster of 30 spins using the TPQS algorithm. Our results are shown in Fig. 11. They closely resemble those of the BBK model: a strong peak below 1 K, and a diminished broad peak around 3 – 5 K. Hence we see that the predictions of the coupled hexagon model deviate from the experimental data in much the same way as those of the BBK model, and thus the coupled hexagon model does no better than the BBK model at reproducing the experimental specific heat capacity for a small cluster of spins.

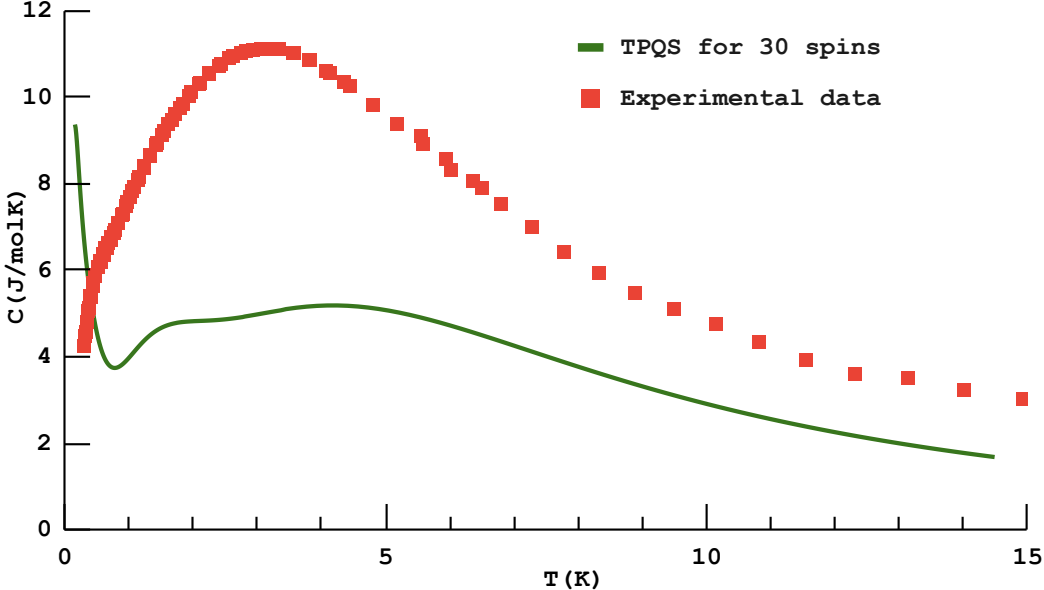


FIG. 11. The zero-field magnetic specific heat capacity of the coupled hexagon model for  $\text{Ca}_{10}\text{Cr}_7\text{O}_{28}$ . We performed the calculation for a cluster of 30 spins using the Thermal Pure Quantum States algorithm (green curve). This model was first presented by Balz *et al.* in ref. [11]. The experimental zero-field specific heat capacity of  $\text{Ca}_{10}\text{Cr}_7\text{O}_{28}$ , previously published in ref. [11], is given for reference (red squares).